APPLICATION OF THREE-COMPONENT PIV TO A HOVERING ROTOR WAKE

James T. Heineck
Experimental Physics Branch
NASA Ames Research Center
Moffett Field, CA

Gloria K. Yamauchi
Army / NASA Rotorcraft Division
NASA Ames Research Center
Moffett Field, CA

Alan J. Wadcock
Aerospace Computing, Inc.
Los Altos, CA

Luiz Lourenco
Florida State/Florida A&M University
Tallahassee, FL

Anita I. Abrego
Army / NASA Rotorcraft Division
NASA Ames Research Center
Moffett Field, CA

Abstract

Three-component velocity measurements in the wake of a two-bladed rotor in hover were made using the Particle Image Velocimetry (PIV) technique. The velocity fields were oriented in a plane normal to the rotor disk and were acquired for wake ages ranging from 0 to 270 deg. for one rotor thrust condition. The experimental setup and processing of the instantaneous images are discussed. Data averaging schemes are demonstrated to mitigate the smearing effects of vortex wander. The effect of vortex wander on the measured vortex core size is presented.

Introduction

The key to accurate predictions of rotorcraft aerodynamics, acoustics, and dynamics lies in the accurate representation of the rotor wake. The vortical wakes computed by rotorcraft CFD analyses typically suffer from numerical dissipation before the first blade passage. With some *a priori* knowledge of the wake trajectory, grid points can be concentrated along the trajectory to minimize this dissipation. Comprehensive rotorcraft analyses based on lifting-line theory rely on classical vortex models and/or semi-empirical information about the tip vortex structure. Until the location, size, and strength of the trailed tip vortex can be measured over a range of wake ages, the analyses will continue to be adjusted on a trial and error basis to correctly predict blade airloads, acoustics, dynamics, and performance. Using the laser light sheet technique, tip vortex location can be acquired in a straightforward manner. Measuring wake velocities and vortex core size, however, has been difficult and tedious using point-measurement techniques such as laser velocimetry. The Particle Image Velocimetry (PIV) technique has proven to be an efficient method for acquiring velocity measurements over relatively large areas and volumes for rotating flow-fields. The majority of PIV work reported to date has been restricted to 2-component velocity measurements acquired from the wake of a rotor in forward flight (Refs. 1-12). Ref. 10 describes an experiment where three-component velocity measurements were made on a rotor in forward flight, although only preliminary results are shown. Although PIV has become an increasingly favored technique for acquiring flow field information on rotor wakes, there has been minimal information in the literature regarding methods of extracting critical parameters such as vortex core size and strength from PIV data.

The present work had two objectives. The first objective was to gain experience in applying the three-component (3D) PIV technique to a simple rotor configuration. A two-bladed, untwisted rotor operating at moderate thrust in hover was selected for this investigation. Restricting the test conditions to hover allowed greater freedom, compared to forward flight testing, in locating the cameras and laser sheet. Three-component PIV permits both cameras to be positioned in the forward scatter position relative to the laser light sheet thereby maximizing the quality of the particle images. The second objective was to

Presented at the American Helicopter Society 56th Annual Forum, Virginia Beach, Virginia, May 2-4, 2000.

obtain vortex core size and document the effects of vortex wander.

This paper provides a description of the test facility and the model used for the experiment, a discussion of the test conditions, a detailed description of the PIV measurement set-up, and the data processing technique and procedures. Specific findings from this experiment are discussed.

Facility and Model Description

The experiment was performed at NASA Ames Research Center in the U.S. Army Aeroflightdynamics Directorate Hover Test Chamber. The following sections describe the test chamber and rotor model.

Hover Test Chamber: The chamber floor is 26 ft x 32 ft. The chamber ceiling height is adjustable and was positioned approximately 6 ft above the rotor hub for this experiment (Fig. 1(a)). Two large roll-up doors on opposite sides of the chamber were each raised 32 inches to allow the rotor to draw in air from the outside. Air filters were used to minimize debris entering the chamber from beneath the roll-up doors. The rotor wake was exhausted upward through an aperture in the chamber ceiling and then to the exterior through openings near the top of the chamber.

Test Stand and Rotor: Fig. 1(b) shows the two-bladed rotor and the Rotary Wing Test Stand (RWTS) installed in the hover chamber. The RWTS has two 90-HP electric motors and a 2.5:1 transmission. A flexible coupling between the input shaft and dummy balance was instrumented to measure torque. A rotary shaft encoder served to provide the synchronization trigger for the PIV cameras and laser.

A two-bladed rotor was installed on the RWTS. The blades have a rectangular planform, zero twist, and a chord of 7.5 inches. The rotor diameter is 7.5 ft. The outer 50 percent of each aluminum blade is a NACA 0012 profile; the profile linearly tapers to a NACA 0020 from 0.5R to 0.2R (Ref. 13). The rotor hub consists of 2 steel halves which are clamped together to hold the blades at the desired pitch setting. The hub-and-blade assembly is designed for a zero-degree coning angle. To minimize recirculation in the chamber, blade pitch was manually adjusted to a negative angle resulting in a downward thrust and upwardly convected wake. The rotor hub was approximately 7.5 ft above the chamber floor. A similar installation was used in Ref. 13, which provides additional details about the rotor and test stand.

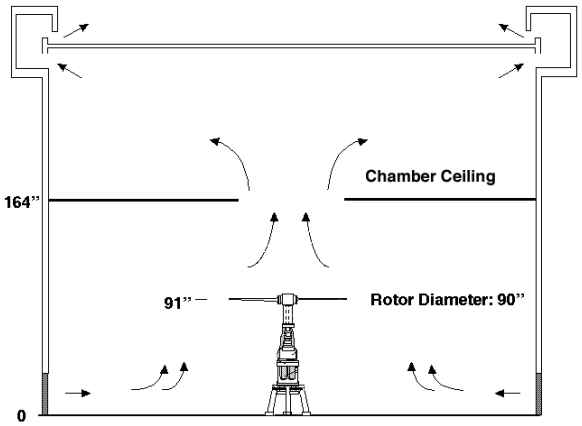

Fig. 1(a). Illustration of test stand and chamber.

Fig. 1(b). Photograph of test stand installed in hover chamber.

Fig. 1. Hover chamber test installation.

Test Conditions: Rotor rpm was chosen to be 870 rpm (14.5Hz) to maximize the thrust while not exceeding the maximum frame rate of the PIV cameras. Since a rotor balance was not installed for this test, a thrust condition matching the condition tested in Ref. 13 was selected. All data were therefore acquired for –8 deg. collective pitch, corresponding to a rotor thrust coefficient of 0.005. PIV data were acquired from 0 deg. to 270 deg. wake age in increments of 30 degrees. Five hundred image pairs, or realizations, were recorded in groups of 50 at each wake age.

Three-Component PIV Method Description

PIV measures fluid velocities by time-sequential imaging of individual tracer particles in the flow. A laser light sheet illuminates the particles. The cross-

correlation of two successive images yields the magnitude and direction of the particle displacement.

Originally, PIV was developed using a single camera that viewed the laser light sheet normal to the plane. The resulting data was an array of two-component velocity vectors. One error source in 2D PIV is caused by out-of-plane motion of the particles. Near the center of the image area, where the view angle is nearly 90 deg. to the plane, the error is negligible. Toward the edges of the image the view angle decreases from the ideal 90-deg. angle such that the motion perpendicular to the sheet becomes detectable. This perspective error led the PIV community to believe that the method was sensitive enough to exploit the so-called out–of-plane error to derive the third component of velocity (Ref. 14). By using two cameras to view the laser sheet obliquely, the movement through the laser sheet can be recorded. Each camera has a different perspective of the particle motion from Ref. exposure (T_0) to Delayed exposure (T_1) in the region of interest (Fig. 2). The third component of velocity can be calculated using photogrammetric equations. The method became known as Stereoscopic PIV or 3D PIV.

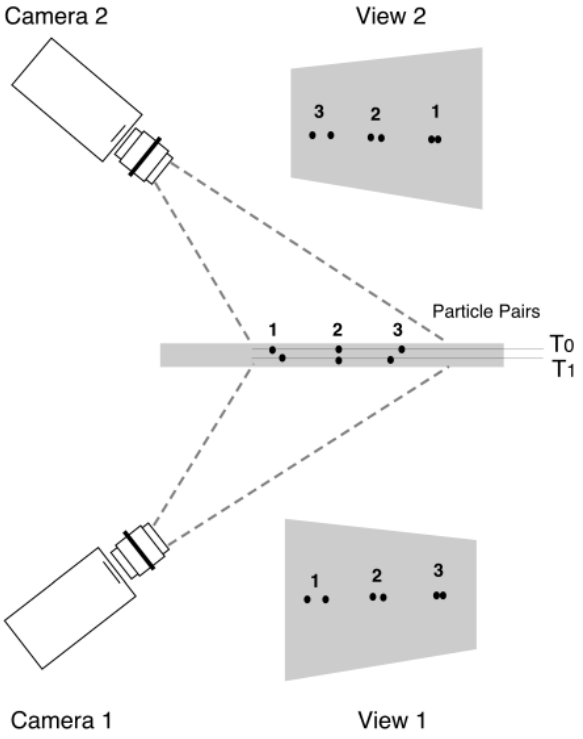

Fig. 2. Diagram showing the perspective effect of particles in 3D motion for Stereoscopic PIV.

The technique demands both critical focus and maximum brightness of the particle image. Conventional lens mounts create a plane of focus in object space that is parallel with both the image plane and the lens plane. An optical challenge arises when the camera views the plane of laser light obliquely. Using conventional focusing, a small lens aperture (large f value) is required to produce the large depth of field necessary to maintain discrete particle images. Unfortunately, a small lens aperture drastically reduces both the particle image intensity and image resolution. For this reason a new approach was necessary.

Scheimpflug focusing solved this conundrum. (Ref 15). Fig. 3 illustrates the basic principle, which states that when the object plane, the lens plane and the image plane meet on a common line in space, focus is achieved. Photogrammetic equations were derived specifically for 3D PIV using the Scheimpflug technique (Ref. 16).

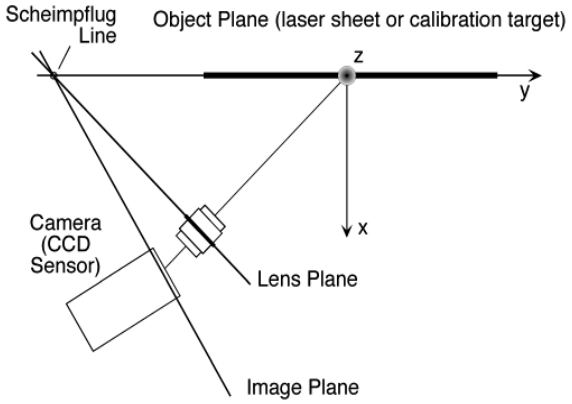

Fig. 3. The Scheimpflug condition.

Experimental Set-up

The cameras were mounted horizontally on a plane 3 inches above the rotor disc. Fig. 4 shows an overview of the system. The angle of view for each camera relative to the laser light sheet was 36 deg. This angle maximized the brightness of the particle image by capitalizing on the efficiency of laser light in forward-scatter without sacrificing accuracy. Fig. 5 illustrates the position of the image area relative to the blade tip. The image height is twelve inches outboard and approximately 16 inches inboard due to perspective. The radial extent of the flow field covered is about 18 inches.

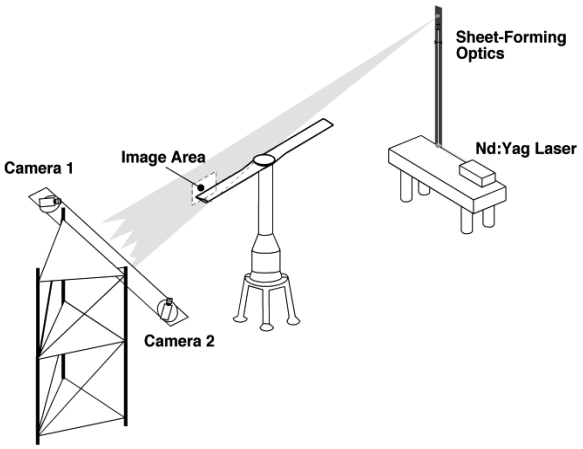

Fig. 4. Overview of PIV system set-up.

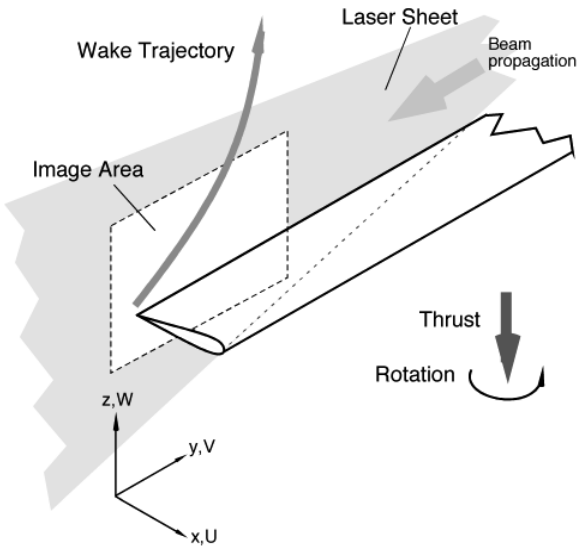

Fig. 5. Diagram of image area and orthogonal axes.

Camera Set-up: Kodak ES 1.0 cross-correlation cameras were used for image acquisition. This model has a double-exposure mode that permits two non-interlaced full-frame images to be acquired in a single frame interval. The time interval between images can be as short as 2 microseconds or as long as 30 milliseconds. Since they are not standard video cameras they can be externally triggered and driven at any frequency up to 15 Hz in the double-exposure mode. These cameras have 8-bit CCD arrays of 1008(h) x 1018(v) pixels. Each pixel measures 9 µm on a side. The camera has remote-adjustment capability for digital gain, contrast, black-level and trigger mode through the computer interface.

The cameras were positioned on a horizontal platform an equal distance on either side of the laser sheet. Each camera assembly was mounted on a turntable to permit coarse alignment of the camera view. Each assembly used a Nikon 55 mm f1.2 lens. The lens was mounted on a micrometer-driven two-axis translation stage, which permitted fine adjustment of the image position. The lens and two-axis stage were mounted on a motorized linear-translation stage. The camera was mounted on a motorized rotation stage. Fig. 6 shows the assembly without the bellows between the camera and lens to illustrate the angular adjustment. All four stages were remotely operated through a single controller thus providing real-time focus control. By rotating the camera and translating the lens, the Scheimpflug condition could be satisfied.

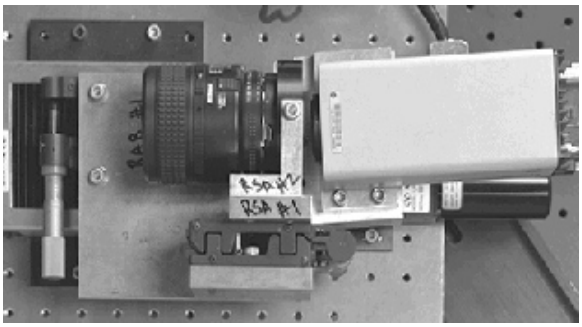

Fig. 6. Photograph of the camera assembly.

Laser and Sheet Optics: The laser used for this experiment was a Spectra Physics PIV-400 model. The pulse duration of this laser is 9 nanoseconds with 350 millijoules per pulse in the 532-nanometer band. The beam diameter is 9mm with a divergence of 0.50 millirads. All mirrors and optics used had laser damage thresholds of no less than 1J/cm^2.

A positive 200-mm and a negative 200-mm cylindrical lens pair, mounted colinearly, controlled the sheet thickness. By adjusting the distance between these lenses, the waist of the focal point could be projected to the optimum location in the field of view. The laser sheet thickness varied slightly from 0.8 mm in the center to 1.1 mm on the edges of the image area. A negative 75-mm cylindrical lens was used to spread the beam vertically to form the light sheet. The laser sheet was projected from a distance of approximately 25 feet, over the rotor hub, to the region of interest as shown in Fig. 7.

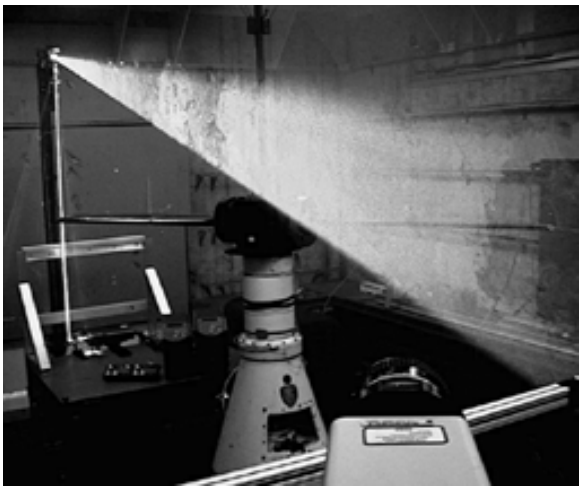

Fig. 7. Photograph of region of interest from Camera 1 position.

System Alignment: The primary blade was positioned at the zero-degree reference point and a calibrated laser level (sweeping type) was used to establish the vertical plane through the blade trailing edge. The Nd:YAG laser was directed through the optics, adjusted for thickness, steered to the blade trailing edge and adjusted to the vertical plane defined by the sweeping laser level. The calibration target was placed at the blade trailing edge such that the image area spanned from three inches below the blade trailing edge to nine inches above and 2.5 inches outboard of the blade tip to about 15 inches inboard. The target was leveled to 0.01deg. using a digital inclinometer. Measurements of the blade-tip location with respect to the target were made to ±1/32". The YAG laser was directed toward the target as a final check. When the laser light sheet evenly grazed the surface of the target, the target alignment was satisfactory. The target was illuminated with white light on both sides, the cameras were focused and calibration images were recorded.

PIV Software: This experiment was performed using the Integrated Design Tools (IDT) WinVu v5.10 software. This software functions as both a data acquisition interface and an image-processing interface. This has the advantage of providing a fully integrated calibration procedure that allows for acquisition, quality assurance and data reduction. The calibration yields all the optical parameters required for accurate reconstruction of three-component velocity-vector fields (Ref 17). The calibration is performed both before and immediately after each run.

The first step in processing images is to define the region of interest in the image with an interrogation grid. The intersections between the vertical and horizontal grid lines define the centers of each interrogation window. The interrogation window is the smaller region in the reference and delayed images that are cross-correlated using an optimized Fourier transform. When the camera calibrations are applied, the grid in each camera view covers the exact same area in the flow field.

The interrogation window size is then chosen based on the particle density and the maximum instantaneous displacement of the particles. Typically the window size ranges from 8 to 64 pixels on a side. Each interrogation window yields one vector. The cross-correlation of the interrogation window in the reference image with that of the delayed image yields a correlation map. The location of the correlation peak in space determines the local displacement in both magnitude and direction. A mathematical description of the WinVu algorithm can be found in Ref. 17.

Uniform seed density is of paramount importance to the accuracy of the measurement. WinVu incorporates a quality assurance test in the vector calculations. First, the software counts the number of particles in the interrogation window. Nine particles are required to contribute to a correlation map. It is assumed that all particles in an interrogation area are moving identically, so that a simple average over all the particle motions reduces the statistical measurement error by 1/3.

If there are enough particles, the processing begins with a first-pass correlation between the reference image and delayed image to determine the maximum displacement range. For the second pass the software enlarges the interrogation area in the delayed image. The amount of the enlargement is based on the maximum displacement range determined in the first pass. Since the Fourier transform requires both interrogation areas to be identical, the software "adds zeros" to the interrogation area of the reference image to match the size of the delayed image area. This technique maximizes the probability of correlating all the particles found in the reference image interrogation area to those found in the delayed image, thereby maximizing the statistical accuracy.

If there are not enough particles in a given interrogation region, the program will automatically enlarge the interrogation area of the reference image. If there are nine or more particles in this enlarged area, then the correlation proceeds in the same manner described above. The data for this grid point is considered to be a recalculation. If nine particles are not counted, the software will expand the interrogation area incrementally. It will repeat this process until the interrogation area expands to a limit of 64x64 pixels. If the nine-particle threshold is not met for the largest area, then velocity values are interpolated for that grid point using a second-order curve fit based on nearest-neighbor values. This vector is also counted as a recalculation.

The software tracks the number of these recalculations and displays that number after each camera view is processed. If the number of

recalculations is less than 1% of the total vectors then the data are considered reliable.

Calibration Procedure: The calibration target shown in Fig. 8 was designed for the calibration procedure required by the WinVu software. The target consists of two digitally generated photographic prints, one the mirror image of the other. The two prints were mounted back-to-back after careful registration on a light-table. The target is large enough to occupy the entire 12 inch by 18 inch (30 mm x 45 mm) region of interest. The target contains three concentric squares and an outer perimeter rectangle. Each square was measured using a Cordax two-axis Optical Probe inspection system. This device is used for specification compliance testing for precision machining. It measures to an accuracy of 0.0001 of an inch (2 to 3 microns). The calibration routine uses the dimensions of any one of the boxes to establish the magnification ratio and perspective correction parameters. The background pattern simulates a particle field which is used to focus and to provide an end-to-end check of the system. The background can be treated like a particle image field to correlate images recorded in the displacement procedure described below.

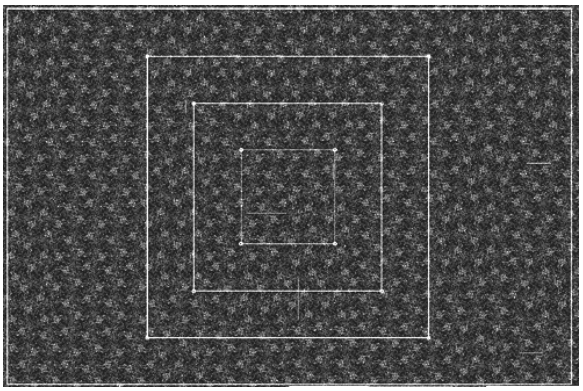

Fig. 8. Target image for in-situ camera calibration.

System Accuracy: System accuracy is determined by displacing the calibration target a precise amount and measuring that shift using the PIV system. Raffel *et.al.* (Ref. 18) has shown this method to provide the best estimate of system accuracy. Alternative methods include statistical analysis of optical parameters (Ref. 19) and the measurement of a "known" flow.

The target was mounted on a three-axis linear translation stage. Manual micrometers, calibrated to 0.0001 inch (2 to 3 microns) on the Cordax system, drove each axis of translation. An image of the target was recorded after each axial translation. The respective images were processed in WinVu using the simulated particle field shown in Fig. 8. Table 1 presents results from displacing the calibration target in each of the three directions. The mean displacements were derived from approximately 3800 vectors. The relatively large displacement of 0.200 inches (5.080 mm) in each orthogonal direction was chosen to minimize any error associated with the micrometers. The average error in displacement for the x, y, and z directions is 1.2%, 0.26%, and 0.47% respectively. As expected, the largest error is associated with the out-of-plane displacement (x).

It is unlikely that the flow-field measurements have the same percent accuracy. Rather, it is more likely that the absolute error is independent of displacement magnitude. The displacements chosen for this procedure are typically three times larger than the displacements found in actual flow-field images. Thus, the percentage error for the PIV measurements may be up to three times higher. Table 1 shows the analysis of the static displacement procedure.

Direction	Actual displacement (mm)	Measured displacement and error (mm)	Measurement std. dev. (mm)
x	5.080	5.017, -0.063	0.059
y	5.080	5.056, -0.024	0.018
z	5.080	5.067, -0.013	0.024

Table 1. Error analysis from static-displacement procedure.

Flow Seeding: Seeding of the flow is of critical importance in PIV applications. The seed must follow the flow without altering or lagging behind it. The seeding material must mix thoroughly with the flow such that images have uniform seed density over the entire image area. The smaller the particle, the better the mixing and flow tracking (Ref. 20). It is highly advantageous to have real-time remote control of the density of the seed. A Corona Integrated Technologies Vi-Count 5000 smoke generator was used for this experiment. The smoker was operated remotely by a toggle switch located at the data acquisition station. It produces particles of 0.2 to 0.3 microns in diameter using non-toxic, pharmaceutical-grade mineral oil.

The smoker was placed on the floor of the hover chamber. During rotor operation, air drawn through the filters beneath the roll up doors mixed with the seed generated from the smoker. Data images were acquired only after the seed was nearly homogenous in the chamber.

Data Acquisition

The PIV cameras were each connected to separate Imaging Technology IC- PCI frame grabbers installed in a PC workstation. Image acquisition was performed using WinVu enabling efficient, real-time assessment of image quality. Sample images were acquired and processed to optimize image quality and inter-pulse time delay.

A successful PIV measurement is highly dependent on the quality of the raw images. Issues such as background light contamination, image brightness, contrast, focus, beam alignment and light pulse separation bear on the success of image correlation.

Fine focusing and beam-alignment were performed using a seeded jet prior to testing. The jet was a small blower whose intake drew from the ambient air mixed with the smoke. Focusing was accomplished using the remotely operated translation stages while observing the real-time display. The gain and black-level were then adjusted to maximize contrast and brightness of the particle field. To check for laser sheet coplanarity, the motion of the particles was observed on the real-time display where both laser pulses were recorded in one image. As the beams came into alignment, the particle images appeared as doublets.

The final parameter, the inter-pulse time delay, has to be determined under actual test conditions. Sample images are acquired and processed in near real-time. Adjustments to the time delay are made based on the resulting correlation. The most important information required for determining the time delay is the maximum instantaneous displacement. It represents the highest velocity in the flow for a given component and should be optimized to lie in the range of +/-3 pixels, independent of window size. This range maximizes the measurement accuracy. A smaller pixel displacement limits the dynamic range of the measurement (Ref. 19). Displacements that are too large decrease the probability of correlation. The chosen time delay of 40 microseconds produced three-pixel displacements near the vortex core, the region of highest in-plane velocity.

Once image quality was assured, 500 image pairs were acquired per wake age. Each wake age represents 2 gigabytes of raw image data. Image data for ten wake ages were acquired in four hours of operation.

Post-Test Data Processing

Several steps are required to extract vortex structure from the particle images. The following sections describe the procedures used to convert the images to three-component velocity fields, identify the vortex centers and average the velocity fields.

Instantaneous Velocity Fields: A 24x24 pixel cross-correlation window was chosen to process this data set. This dimension was determined by processing sample images using several window sizes. This window size permitted high spatial resolution while ensuring that the required number of particles was present in each window. The interval chosen between adjacent interrogation windows created a 50% overlap in each direction, resulting in a vector field of size 80 x 64. This corresponds to 5180 vectors per instantaneous vector field. The y (radial) grid interval is 5.4 mm in the flow region and the z interval is 3.8 mm. The correlation window size corresponds to 10.8 mm x 7.6 mm in the flow region

Averaging of the Velocity Fields: Two methods for averaging the 500 instantaneous velocity fields were used in this study. The first method does not account for the effect of vortex wander while the second method does.

Method 1: Simple Average: This method performs a simple ensemble average of all 500 instantaneous velocity values at each grid point. The result ignores any vortex wander. If the amplitude of vortex wander is great, the vortex core will be smeared using this approach. Any vortex core measurement based on the mean flow field will be in error. This approach should be in agreement with point-wise measurement techniques such as LDV.

Method 2: Vortex Alignment Average: To mitigate the effects of vortex wander, a scheme to align the velocity fields based on the locations of the vortices prior to averaging was developed. Two methods were used to locate the center of the vortex: the peak vorticity or the midpoint of the locations of the velocity extrema on a diametral profile.

A LabView program was written to calculate vorticity in the x direction (ω) from each instantaneous velocity field using the following central-difference equation:

$$\omega_{i,j} = \frac{\left(W_{i+1,j} - W_{i-1,j}\right)}{\left(y_{i+1} - y_{i-1}\right)} - \frac{\left(V_{i,j+1} - V_{i,j-1}\right)}{\left(z_{j+1} - z_{j-1}\right)}$$

where $\omega_{i,j}$ is the vorticity at grid point (y_i, z_j), $V_{i,j}$ is the radial velocity and $W_{i,j}$ is the vertical velocity component (refer Fig. 5 for axis orientation). The grid point with the highest vorticity is assumed to locate the vortex center. In this experiment each velocity field typically contains two vortices. Each field was therefore divided into two regions with one vortex per region. The velocity fields were shifted to align vortex centers prior to averaging with the mean vortex location.

Results and Discussion

Instantaneous vs. Averaged Velocities: Fig. 9 presents a single instantaneous realization of the flow field consistent with the image area shown in Fig. 5. Fig. 9(a) shows in-plane velocities as vectors with associated contours of out-of-plane velocities, where positive x is toward the reader. For clarity, the figures show only one-fourth of the total calculated vectors. Fig. 9(b) shows the same in-plane vector field with the associated contours of out-of-plane vorticity. Two vortices are clearly definable in the flow field. The vortex in the lower left corner corresponds to a wake age of 30 deg. The vortex in the upper right corner corresponds to a wake age of 210 deg. The horizontal streak in the center of Fig. 9(a) represents the velocity defect associated with the blade wake.

Fig. 10 presents the results of a simple average of the data from the same test conditions of Fig. 9. In the course of processing, 14 vector fields were eliminated due to recording errors or poor seeding. The simple average was performed with the remaining 486 instantaneous vector fields, ignoring any effects of vortex wander. Comparing the instantaneous flow field in Fig. 9 with the mean flow field of Fig. 10 several features are evident. First, the simple average computes out-of-plane velocities and vorticity that are much lower than their instantaneous counterparts. Second, the trailed blade wake is still visible in Fig. 10(a) but the average velocity defect in the blade wake is considerably smaller than shown in Fig. 9(a). These differences can be attributed to vortex wander, as will be demonstrated in the following sections.

Vortex Wander Effects: Fig. 11 illustrates the amplitude of vortex wander observed at 30 deg. and 210 deg. wake ages. The vortex centers, defined as the location of maximum instantaneous vorticity, were plotted for each instantaneous field. Note the increase in amplitude of wander with increased wake age. Fig. 12 shows histograms of vortex location for wake age 210 deg.

To further demonstrate the effects of vortex wander, Fig. 13 presents mean in-plane velocity vectors and contours of out-of-plane vorticity using two different averaging techniques. These figures show all the vectors calculated in this region of the flow field. The vortex wake age of 210 deg. was chosen to emphasize the effects of wander. Fig. 13(a), an expanded view taken directly from Fig. 10(b), shows the simple ensemble average. Fig. 13(b) shows the result of aligning vortex centers prior to averaging. As expected, the simple average has reduced the peak vorticity of the vortex core and redistributed it over a larger area in the flow field. Fig. 13(a) corresponds to the flow field that would be measured by point-sampling techniques such as LDV, hot-wire anemometry and pressure probe measurements. Unlike PIV, these techniques have no means for correcting for vortex wander.

Vortex Core Measurements: The average horizontal vortex core diameter for the 210 deg. wake age is calculated from instantaneous W component profiles of each vortex. The core diameter is determined by measuring the distance between the velocity extrema of the profile. The profiles were drawn horizontally through the vortex center locations determined in the previous section. The average measurement improves if the profiles undergo an alignment procedure. Three methods for averaging are presented. The first method takes a simple average of the velocity values at each line interval. This corresponds to a point-wise measurement technique. The second method aligns the profiles using the maximum vorticity locations determined earlier. The third method aligns the midpoints of the velocity extrema for each profile.

Fig. 14(a) shows several instantaneous profiles without any attempt to align them horizontally. Only ten are presented here for clarity. Fig. 14(b) shows the same ten velocity profiles aligned according to the y-value of the maximum vorticity location. Fig. 14(c) shows the same ten profiles aligned using the center locations determined from the midpoint of the velocity extrema of each instantaneous profile. Fig. 14(d) shows the result of averaging all 486 profiles using the three alignment methods. It is apparent from Fig. 14(d) that identification of the vortex center with the instantaneous peak vorticity is less successful than using the midpoint of the velocity extrema.

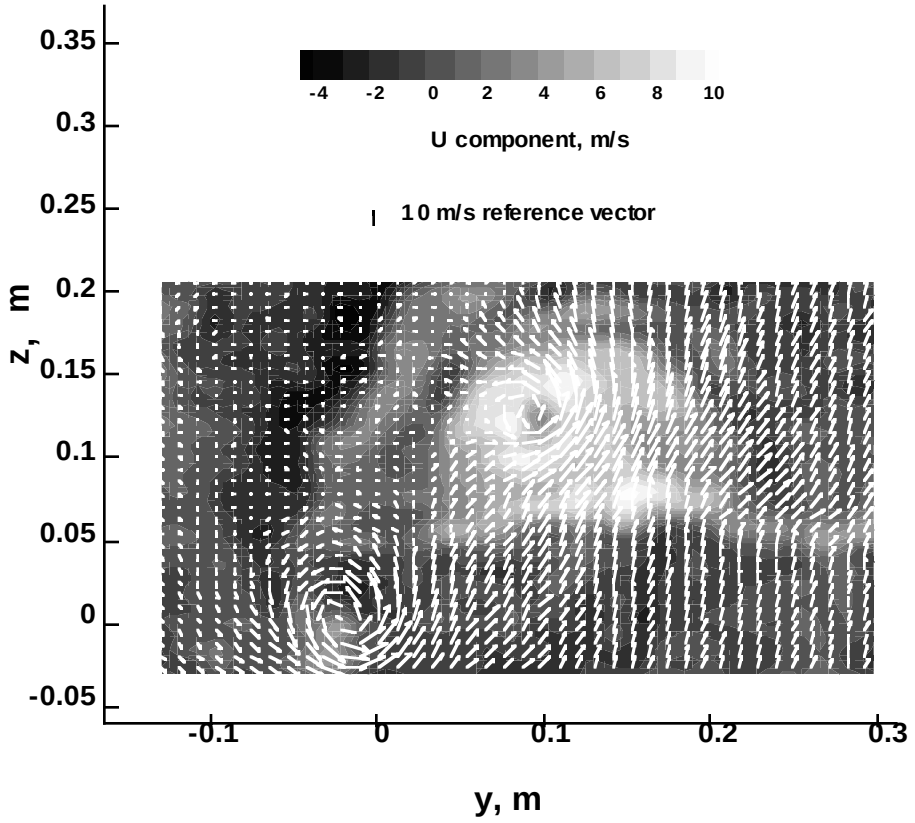

Fig. 9(a). Contour plot of out-of-plane velocity component.

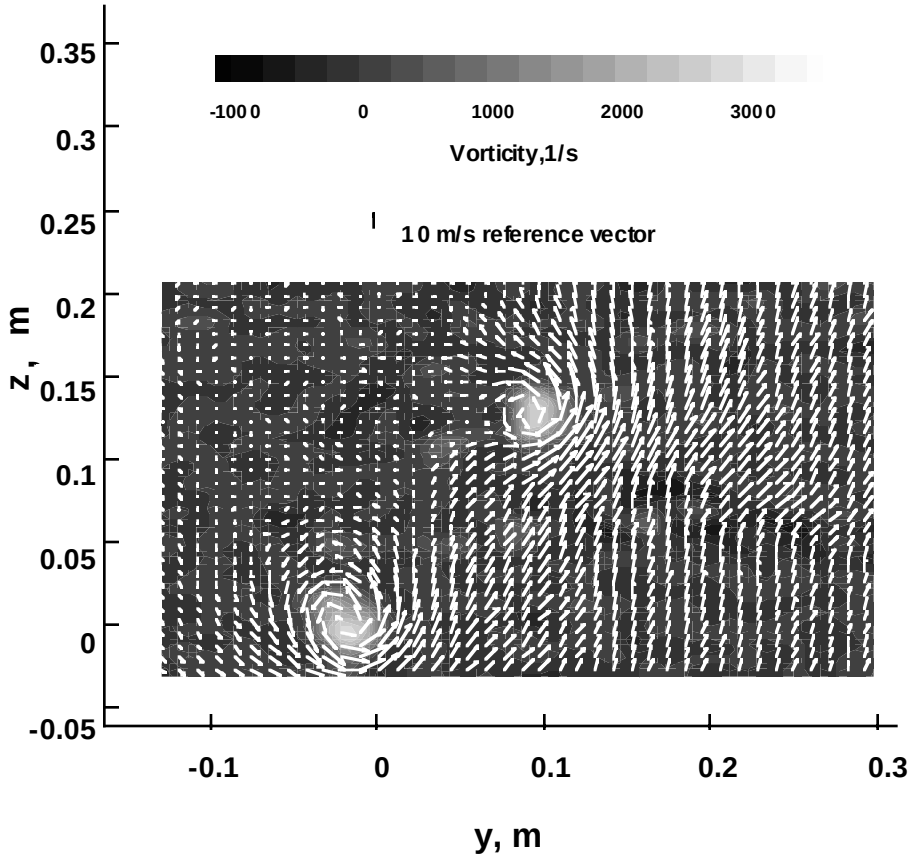

Fig. 9(b). Contour plot of vorticity.

Fig. 9. Instantaneous in-plane velocity vectors with associated contours of out-of-p

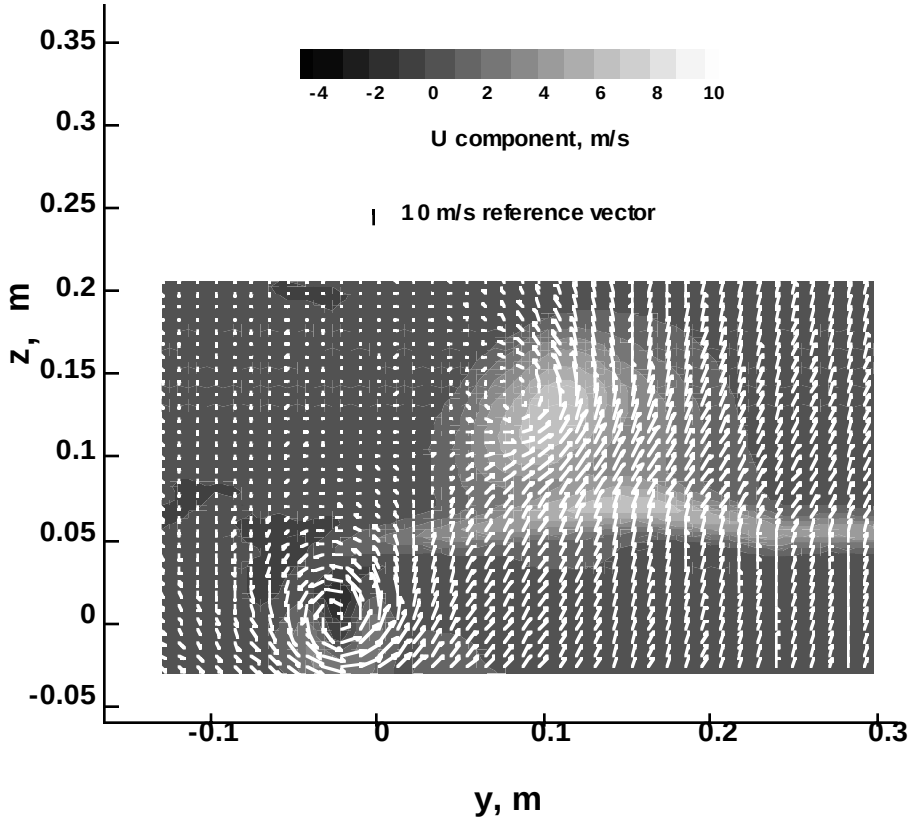

Fig. 10(a). Contour plot of out-of-plane velocity component.

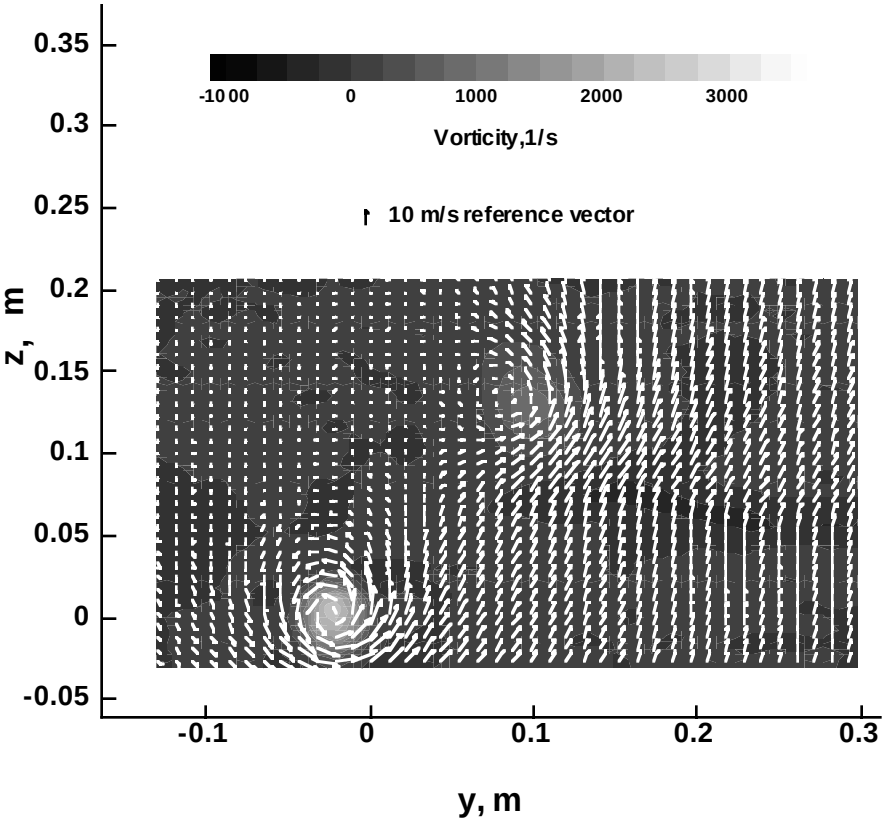

Fig. 10(b). Contour plot of vorticity.

Fig. 10. Ensemble Average showing in-plane velocity vectors and associated contours of out-of-plane velocity and vorticity.

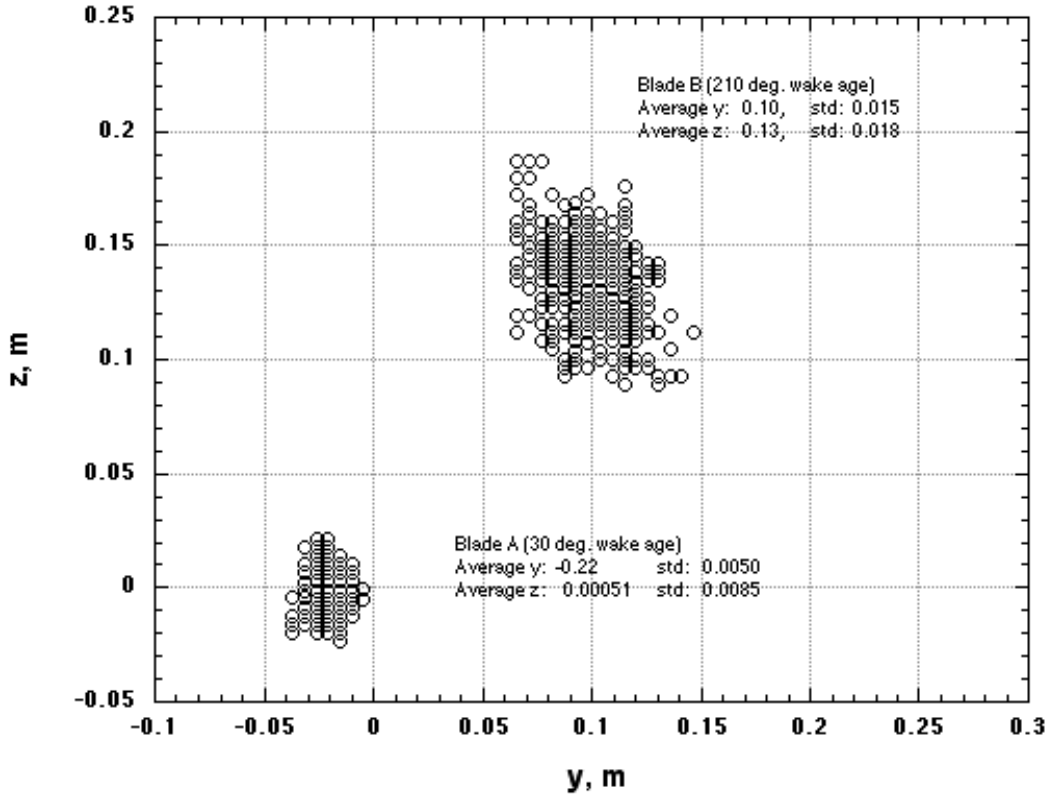

Fig. 11. Instantaneous vortex locations.

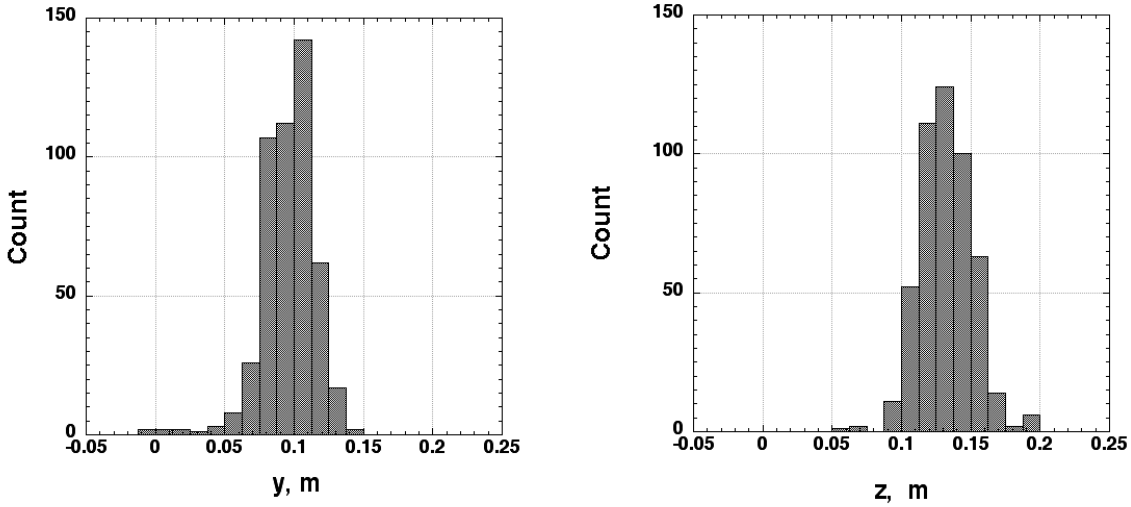

Fig. 12. Histograms of vortex location for wake age 210 deg.

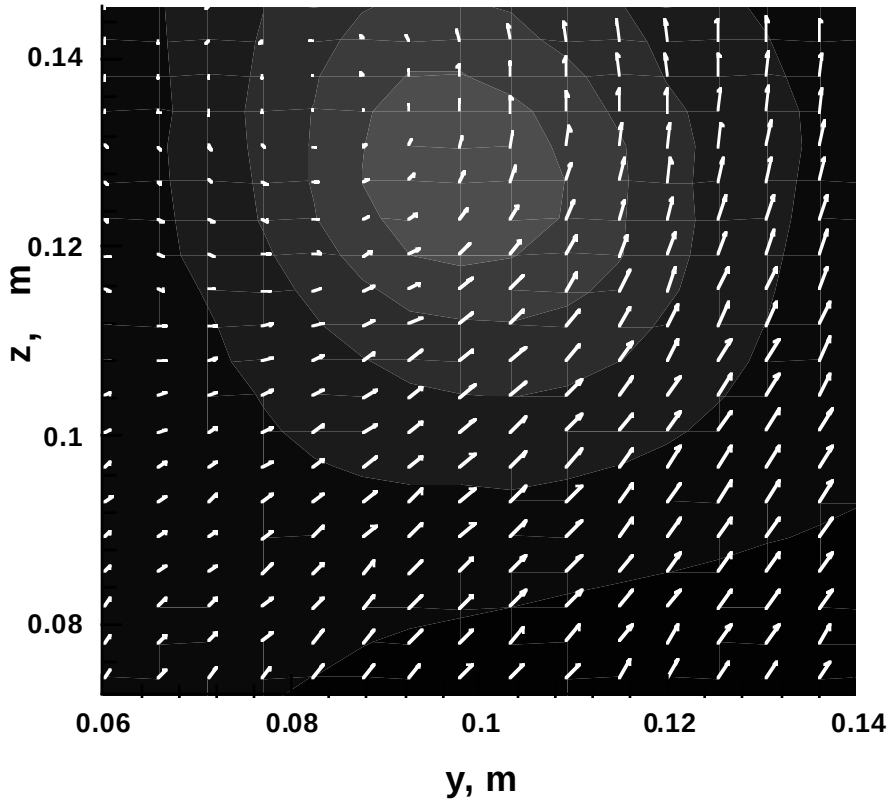

Fig. 13(a). Simple average.

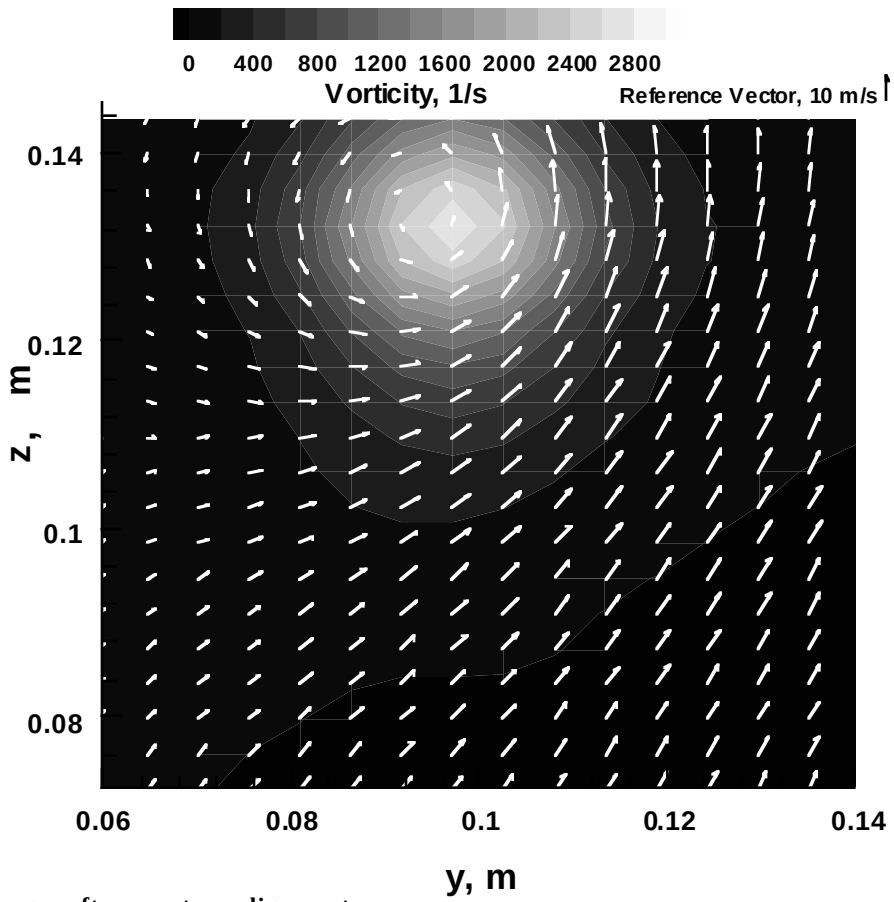

Fig. 13(b). Average after vortex alignment.

Fig. 13. Mean in-plane velocity vectors with vorticity contours for wake age 210 deg.

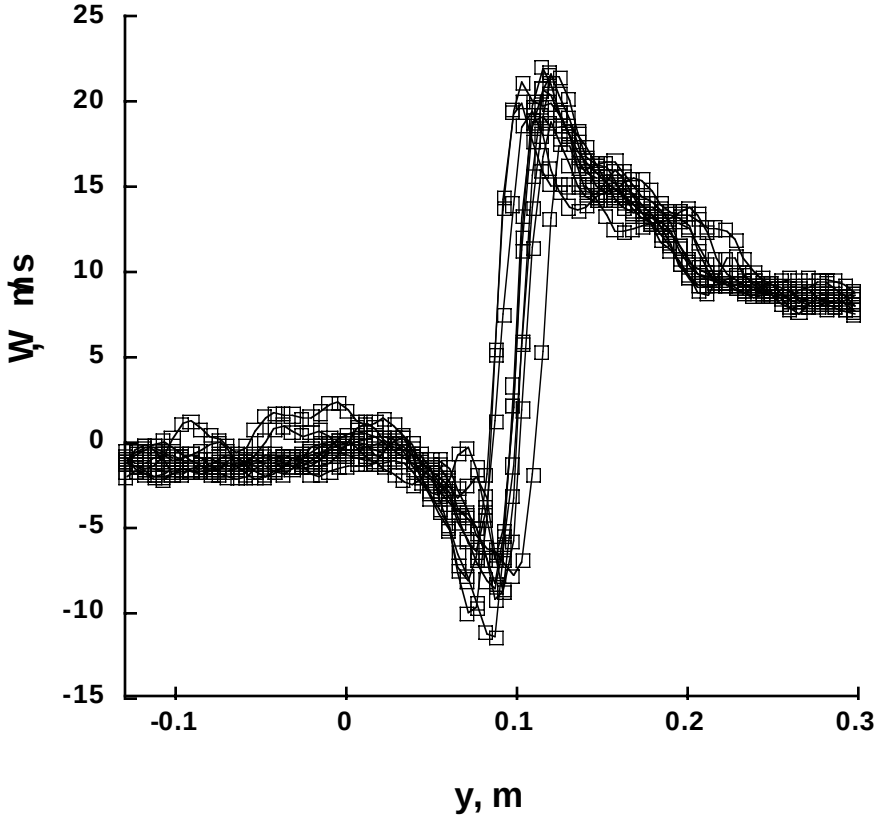

Fig. 14(a). Ten instantaneous horizontal profiles without any re-alignment.

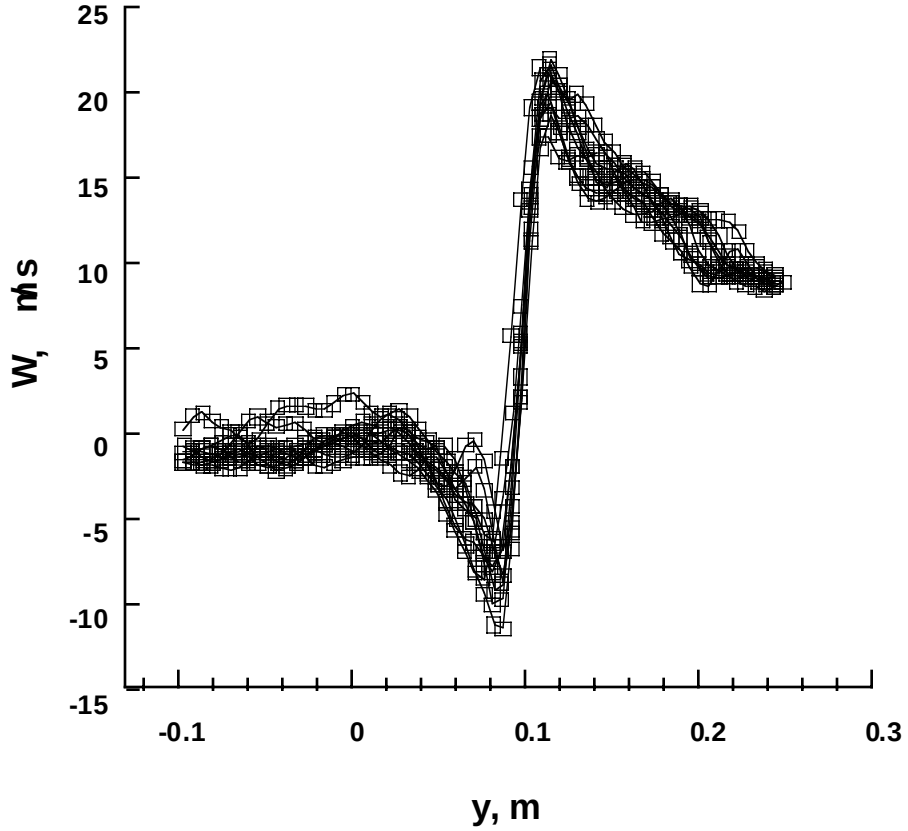

Fig. 14(b). Same ten instantaneous profiles shifted to mean vortex center location based on peak vorticity

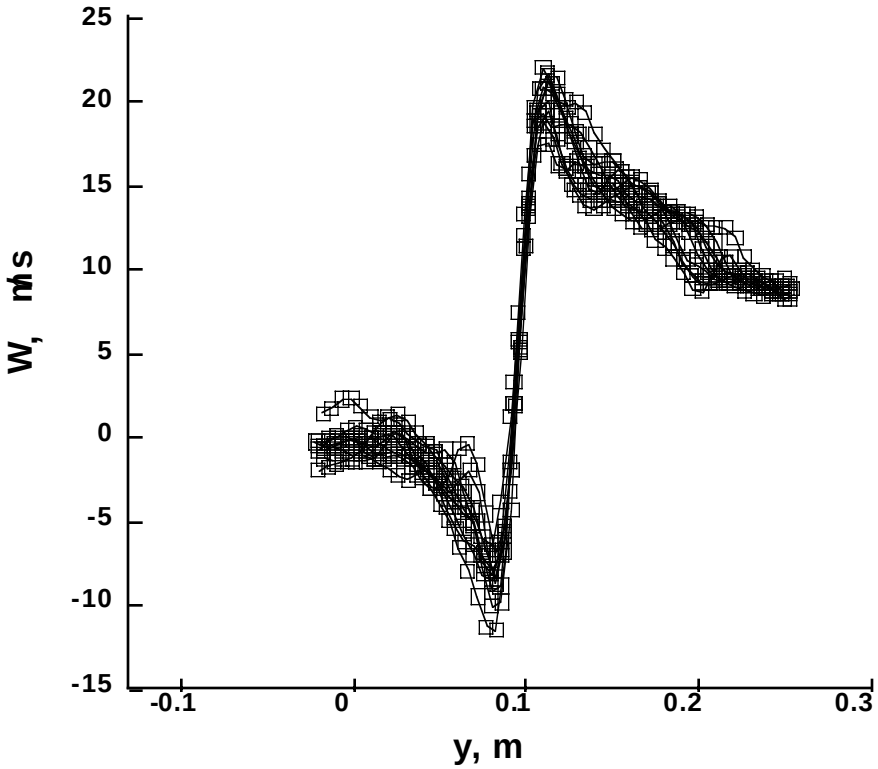

Fig. 14(c). Same ten instantaneous velocity profiles, after alignment, based on the midpoint of the velocity extrema.

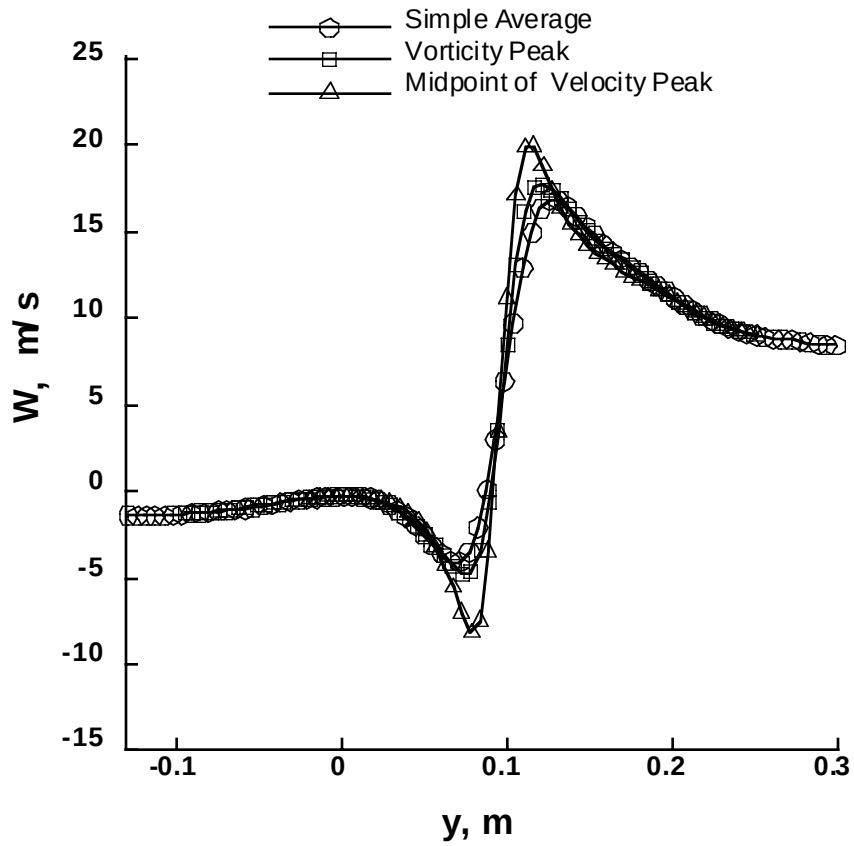

Fig. 14(d). Average velocity distribution through vortex using the three averaging methods.

Fig. 14. Mean velocity distribution through vortex at wake age 210 deg.

It is well known that the vorticity calculation is sensitive to noise in the instantaneous velocity measurements. However, it is not clear how the vortex center can be derived from two-dimensional velocity data employing the tangential velocity extrema method. The convection velocity can influence the tangential velocity. The vorticity of the vortex is not sensitive to the convection velocity, therefore the location of the vortex core though a calculation of instantaneous vorticity appears to be the best approach.

Using a vorticity area-measurement technique may rectify noise-induced errors in locating the vortex core. One method would be to define the centroid of the instantaneous vorticity field as the vortex center. Another method would cross-correlate instantaneous vorticity fields to determine the shift between successive realizations. Also, reducing the noise in the instantaneous vorticity calculations can be accomplished by using a central-difference algorithm that uses five grid points for the two in-plane axis directions instead of three. The disadvantage for each of these routes is an increased computational penalty.

The dimension of the core diameter was determined to sub-grid accuracy by applying a local second-order curve fit to each velocity extremum from1Fig. 14(d). Table 2 presents core diameter measurements from each of the three velocity profiles.Best evidence indicates a core diameter of 34.7 mm (d_{core}/c_{tip}= 18%). The simple average is shown to supply an apparent core diameter of 59.2 mm (d_{core}/c_{tip}= 31%) which is 71% too large due to vortex wander. Note that the root mean square of vortex wander amplitude (Fig. 11) about 17 mm, which is 29% of the apparent core diameter, but 49% of the true core diameter.

	Core diameter(mm)	d_{core}/c_{tip} (%)
Straight Average	59.2	31.1
Max Vorticity Alignment	46.4	24.4
Mid-point Alignment	34.7	18.2

Table 2. Estimate of core diameter at wake age 210 deg.

Conclusions

The wake of a two-bladed rotor in hover has been studied using the three-component PIV technique. The vortex at wake age 210 deg. was chosen to study the effects of vortex wander.

PIV was shown to reveal the instantaneous vortex location, thereby allowing an average flowfield to be computed in a coordinate moving with the vortex. The internal structure of the vortex is thus preserved in the averaging process. Vortex wander effects can therefore be removed from the measurements. The core diameter was found to be 59.2 mm (d_{core}/c_{tip}= 31.0%) using simple ensemble averaging. By aligning the vortex core centers prior to averaging, a more accurate estimate was shown to be 34.7 mm (d_{core}/c_{tip}= 18%).

Acknowledgements

The authors wish to thank Mr. Stephen Walker of NASA Ames Research Center for adapting his vortex location software for this experiment.

References

1. Grant, I., Smith, G. H., Liu, A., Infield, D., and Eich, T., "Measurement of Shed Vorticity and Circulation from a Rotating Aerofoil by Particle Image Velocimetry," 4th International Conference on Laser Anemometry, Advances and Applications, Cleveland, OH, August 1991.
2. Lorber, P. F., Stauter, R. C., Haas, R. J., Anderson, T. J., Torok, M.S., and Kohlhepp, F. W., "Techniques for Comprehensive Measurement of Model Helicopter Rotor Aerodynamics," AHS 50th Annual Forum, Washington, D. C., May 1994.
3. Seelhorst, U., Raffel, M., Willert, C., Vollmers, H., Butefisch, K. A., and Kompenhans, J., "Comparison of Vortical Structures of a Helicopter Rotor Model Measured by LDV and PIV," 22nd European Rotorcraft Forum, Brighton, United Kingdom, September 1996.
4. Horner, M.B., Stewart, J.N., Galbraith, R.A.McD., Grant, I., Coton, F.N., "An Examination of Vortex Deformation During Blade-Vortex Interaction Utilizing Particle Image Velocimetry," 19th Congress of the International Council of the Aeronautical Sciences, Vol. 2, 1994.
5. Coton, F. N., de la Inglesia Moreno, F., Galbraith, R. A. McD., and Horner, M. B., "A Three-Dimensional Model of Low Speed Blade-Vortex Interaction," 20th European Rotorcraft

Forum, Amsterdam, The Netherlands, October 1994.
6. Saripalli, K.R., "Application of Particle Imaging Velocimetry Techniques to Helicopter Rotor Flowfields at McDonnell Douglas Aerospace," 33rd AIAA Aerospace Sciences Meeting and Exhibit, Reno, January 1995.
7. Murashige, A., Tsuchihashi, A., Tsujiuchi, T., Yamakawa, E., "Blade-Tip Vortex Measurement by PIV," 23rd European Rotorcraft Forum, Dresden, Germany, September 1997.
8. Willert, C., Raffel, M., and Kompenhans, J., "Recent Applications of Particle Image Velocimetry in Large-Scale Industrial Wind Tunnels," International Congress on Instrumentation in Aerospace Simulation Facilities, Pacific Grove, CA, September-October 1997 (IEEE Publication 97CH36121).
9. Raffel, M., Willert, C., Kompenhans, J., Ehrenfried, K., Lehmann, G., and Pengel, K., "Feasibility and Capabilities of Particle Image Velocimetry (PIV) for Large Scale Model Rotor Testing," AHS International Meeting on Advanced Rotorcraft Technology and Disaster Relief, Gifu, Japan, April 1998.
10. Murashige, A., Kobiki, N., Tsuchihashi, A., Nakamura, H., Inagaki, K., Yamakawa, E., "ATIC Aeroacoustic Model Rotor Test at DNW," AHS International Meeting on Advanced Rotorcraft Technology and Disaster Relief, Gifu, Japan, April 1998.
11. Yamauchi, G. K., Burley, C. L., Mercker, E., Pengel, K., and JanakiRam, R., "Flow Measurements of an Isolated Model Tilt Rotor," AHS 55th Annual Forum, Montreal, Canada, May 1999.
12. Raffel, M., Dewhirst, T., Bretthauer, B., and Vollmers, H., "Advanced Flow Velocity Field Metrology and their Application to Helicopter Aerodynamics," 24th European Rotorcraft Forum, Marseilles, France, September 1998.
13. McAlister, K. W., Schuler, C. A., Branum, L., and Wu, J. C., "3-D Wake Measurements Near a Hovering Rotor for Determining Profile and Induced Drag," NASA Technical Paper 3577, ATCOM Technical Report 95-A-006, August 1995.
14. Lourenco, L. M., "Particle Image Velocimetry," VKI Lecture Series, Particle Image Velocimetry, 1996-06.
15. Arroyo, M. P. and Greated, C. A., "Stereoscopic Particle Image Velocimetry," Measurement Science and Technology, 2, 1991.
16. Prassad, A. K. and Jensen, K., "Scheimpflug Stereocamera for Particle Image Velocimetry in Liquid Flows," Applied Optics, 34:7092-9, 1995.
17. Raffel, M., Willert, C., and Kompenhans, J., Particle Image Velocimetry, Springer-Verlag, 1998.
18. Melling, A., "Tracer Particles and Seeding for Particle Image Velocimetry," Measurement and Science Technology, Vol. 8, 1997.
19. Westerweel, J. "Theoretical Analysis of the Measurement Precision and Reliability in PIV", Proceedings of the Third International Workshop on PIV'99, 1999.
20. Lourenco, L., "Mesh-Free Second-Order Accurate Algorithm for PIV Processing," proceedings of VSJ-SPIE98, Paper AB079, Yokohama, Japan, December 1998.